energies

MDPI

*Article*

# Model Predictive Control for Wireless Power Transfer in Light Electric Vehicle Charging Using a High-Fidelity Battery Model

**Afraz Ahmad [1,*], Akanksha [1], Prarthana Pillai [2], Ilamparithi Thirumarai Chelvan [1] and Balakumar Balasingam [2,*]**

[1] Department of Electrical and Computer Engineering, University of Victoria, Victoria, BC V8P 5C2, Canada; akankshaa@uvic.ca (A.); ilampari@uvic.ca (I.T.C.)
[2] Department of Electrical and Computer Engineering, University of Windsor, Windsor, ON N9B 3P4, Canada; pillaip@uwindsor.ca
* Correspondence: afrazahmad@uvic.ca (A.A.); singam@uwindsor.ca (B.B.); Tel.: +1-(519)-253-3000 (ext. 5431) (B.B.)

**Abstract**

This paper presents a primary side model predictive control (MPC) strategy for wireless power transfer (WPT) based charging of light electric vehicle (LEVs). A battery simulator develops a model to accurately reproduce constant-current (CC) charging profile from Open Ciruit Voltage (OCV) and State of Charge (SoC) parameters of the battery. This model forms the foundation of the predictive control design, allowing accurate prediction of the charging trajectory while avoiding reliance on secondary-side feedback signals. The WPT system employs a phase-shifted full-bridge (PSFB) inverter with S-S compensation, where the primary-side controller regulates the secondary-side charging current using only primary-side current measurements. In contrast to conventional secondary side control, which is tuned around nominal coupling, requires explicit feedback, and degrades under coil misalignment and parameter variations, the proposed MPC leverages integrated system and battery models to predict future states and optimally adjust the phase shift for robust charging operation. Simulation and experimental validation on a real-time LEV charging prototype under aligned, lateral, and angular misalignment conditions demonstrate significant reduction in current-settling time compared to fixed-gain proportional-integral (PI) and known adaptive feedback controllers for same system, with lower RMS current and reduced current spikes at the battery. On the embedded controller, the proposed MPC executes within approximately 1 µs per 85 kHz PWM cycle, corresponding to less than 10% CPU utilization, confirming its practical real-time feasibility.

**Keywords:** model predictive control; primary-side control; battery modeling; wireless power transfer; phase-shifted full-bridge; light electric vehicle; EV charging

Check for updates

Academic Editor: Lionel Pichon

Received: 5 May 2026
Revised: 28 May 2026
Accepted: 5 June 2026
Published: 9 June 2026

**Copyright:** © 2026 by the authors. Licensee MDPI, Basel, Switzerland. This article is an open access article distributed under the terms and conditions of the Creative Commons Attribution (CC BY) license.

## 1. Introduction

Light electric vehicles (LEVs), such as e-bikes and e-scooters, are increasingly important for sustainable urban mobility due to their low energy consumption and reduced emissions, typically operating at speeds up to 45 km/h [1]. As their adoption grows, efficient and user-friendly charging solutions become essential. Conventional wired chargers suffer from connector wear, inconvenience, and reliability issues, whereas wireless power transfer (WPT) enables contactless energy delivery, improving usability, safety, and long-term robustness, and enabling future dynamic charging concepts [2]. A representative LEV and WPT charging station is shown in Figure 1.

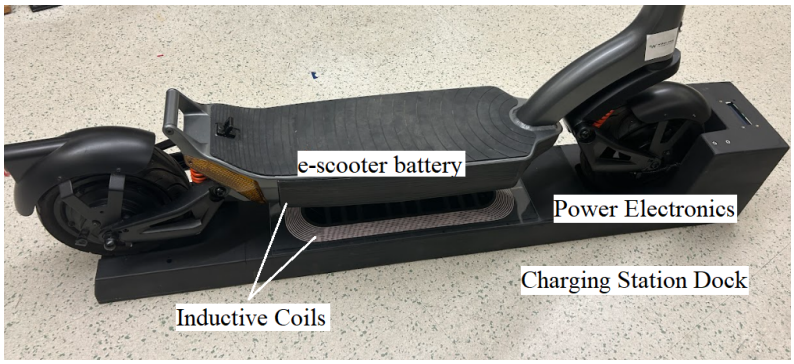



**Figure 1.** E-scooter on a wireless charging station illustrating inductive power transfer between transmitter and receiver coils.

Lithium-ion batteries (LiBs) are the dominant energy storage technology in LEVs due to their high energy density, long cycle life, and fast-charging capability [3]. Their performance depends on cathode chemistry, with LFP, NMC, and NCA widely used in electric mobility, offering different trade-offs between safety, energy density, and cost [4,5]. LEV batteries are typically charged using a constant-current/constant-voltage (CC–CV) profile to ensure safe and complete charging [6]. For the charging interface, magnetically coupled WPT systems are preferred over electric-field or radiation-based methods because they provide higher efficiency and improved safety; practical EV/LEV WPT systems therefore operate in the sub-100 kHz range and follow standards such as SAE J2954 with an 85 kHz nominal frequency [7–9]. A typical inductive WPT system employs loosely coupled coils, a compensation network, a primary-side converter, and a secondary rectifier interfacing the battery, with PSFB converters widely adopted due to their simple structure, fixed-frequency operation, high efficiency, ZVS capability, and reduced RMS current stress [10,11]. SS compensation, rectangular double-layer coils, Litz wire, and appropriate ferrite and aluminium shielding further contribute to misalignment tolerance, reduced current stress, and electromagnetic compatibility, and together define the resonant plant that the control strategy must regulate in LEV charging applications [11–17].

Control of WPT systems is commonly implemented using primary-side, secondary-side, or dual-side strategies to achieve CC–CV charging profiles [18]. Secondary-side control provides accurate regulation but increases onboard complexity, cost, and weight, which is undesirable for LEVs. Primary-side control reduces onboard hardware requirements but often relies on wireless communication for feedback, which introduces reliability concerns under communication loss or interference [19]. To overcome these limitations, parameter estimation from primary-side measurements offers a promising alternative to eliminate continuous communication dependency.

Conventional PI-based controllers are widely used due to their simplicity but suffer from degraded performance under coil misalignment, parameter variation, and nonlinear battery dynamics [20]. Recently, more popular control schemes like Deep Reinforcement Learning (DRL) based Twin-Delayed DDPG for PI tunning has been used in WPT system but they suffer from feedback errors [21]. Model predictive control (MPC) has emerged as a strong alternative due to its fast transient response, constraint handling capability, and robustness to system uncertainties [22]. However, most existing MPC-based WPT approaches still rely on secondary-side sensing or simplified battery representations, limiting practical deployment and increasing system complexity [22].

To address these challenges, this work proposes a MPC scheme for SS-compensated WPT systems in LEV charging. The controller integrates a battery model into the predictive structure, enabling online load estimation and direct computation of optimal phase-shift control using only primary-side measurements. The proposed system is implemented on a

PSFB-based WPT prototype operating at 85 kHz and validated through both simulation and hardware experiments under aligned and misaligned conditions, demonstrating robust constant-current charging without reliance on secondary-side communication.

## 2. System Description

### *2.1. Overall WPT Charging Architecture*

The proposed WPT system is designed to enable contactless charging of LEVs. The overall architecture can be divided into three main stages: a primary-side power conversion stage, a wireless coupling interface, and a secondary-side power conditioning stage. At the input, *ac* power from utility grid is boosted to high-voltage *dc* by a boost power factor correction (PFC) circuit to obtain a stable *dc*-link voltage with minimum eletromagnetic interference (EMI) and Total Harmonic Distortion (THD) level. The *dc*-link voltage is inverted into a high-frequency *ac* for excitation of inductive coils. A compensation network consisting of a capacitor bank is used for compensation of high leakage inductance of the coils on both primary and secondary sides. Power is transferred across the air gap via magnetic coupling between the transmitting ($T_x$) and receiving coils ($R_x$). Diode-bridge rectifier is used for rectifying the high-frequency ac power into *dc* output with a filtering capacitor for charging the battery. Figure 2 shows the overall system architecture from grid-to-vehicle.

In the practical LEV charging station, a wheel sensor in the docking platform detects the presence of the scooter before full-power operation begins. After detection, the system applies a low-voltage test excitation to confirm coil coupling and battery presence based on primary-side impedance changes, and only then enables the rated *dc*-link voltage to the PSFB inverter. During operation, primary-side current is continuously monitored, and if an abnormal rise in input current or a sudden change in the estimated reflected load is detected, the controller rapidly reduces the phase shift and disables the bridge, thereby limiting resonant current in the S–S compensated tank and protecting the MOSFETs.

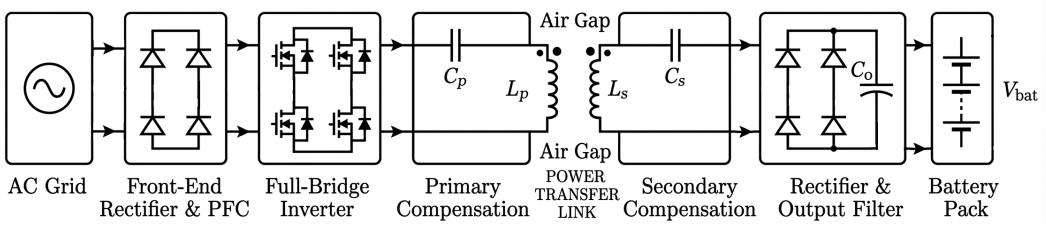



**Figure 2.** Block diagram of the overall wireless power transfer system architecture.

### *2.2. Phase Shift Full Bridge (PSFB) Power Converter*

Figure 3 shows the PSFB converter that implements the high-frequency *dc–dc* stage of the WPT system. The converter is supplied by a regulated *dc* link $V_{dc}$, which is converted into a high-frequency ac excitation by a full-bridge inverter. The inverter consists of four MOSFETs $S_1$–$S_4$, operated at fixed switching frequency and nominal 50% duty ratio, while the transferred power is controlled by phase-shift modulation. A phase shift $\varphi$ is introduced between the gating signals of $S_1$ and $S_4$, which adjusts the effective bridge output and thereby regulates the output current $I_o$ and voltage $V_o$. The resulting inverter output voltage $v_p$ is a bipolar quasi-square waveform.

Using Fourier series expansion, this waveform can be represented as a sum of harmonic components, as shown below:

$$v_p(t) = \sum_{n=1,3,5,\ldots}^{\infty} \frac{4V_{dc}}{n\pi} \cos\left(\frac{n\varphi}{2}\right) \sin(n\omega t). \quad (1)$$

For circuit analysis, only the fundamental component is considered under the fundamental harmonic approximation (FHA), and the inverter output is therefore modeled as an equivalent sinusoidal voltage source. The RMS value of this fundamental component depends on $\varphi$ and is given by:

$$V_{p,\mathrm{rms}} = \frac{2\sqrt{2}}{\pi} V_{dc} \cos\left(\frac{\varphi}{2}\right). \tag{2}$$

This allows the control of the effective excitation applied to the primary side. This excitation drives the primary current $i_p$, which flows through the resonant network and transmitting coil. Figure 4 illustrates the MOSFET gate pulses, including the phase shift between $S_1$ and $S_4$, and the corresponding $v_p$ and $i_p$ waveforms.

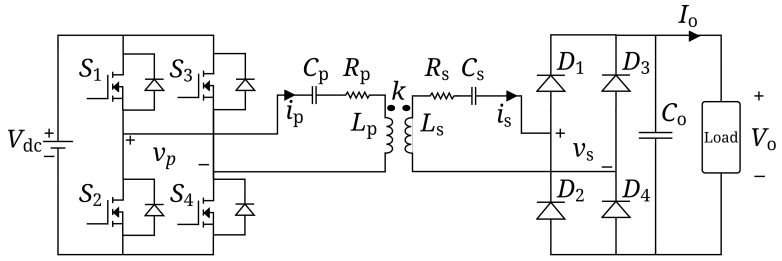



**Figure 3.** Circuit Diagram of Phase Shift Full Bridge (PSFB) *dc-dc* Converter.

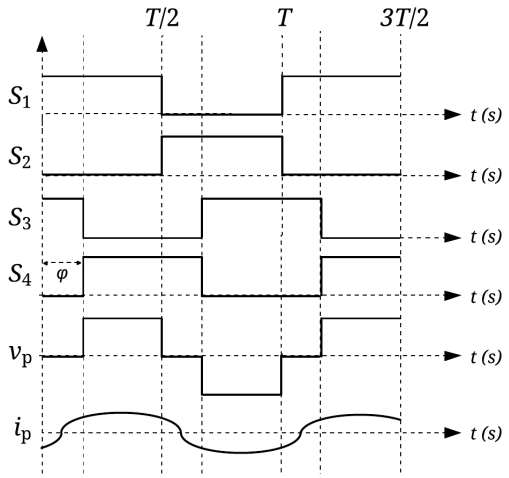



**Figure 4.** Full-bridge gate signals ($S_1$–$S_4$) and corresponding primary-side voltage and current waveforms of the PSFB converter.

### *2.3. Coupled Coils and Compensation Network*

The transmitting and receiving coils form the core of the WPT interface. In this work, both the primary and secondary coils are implemented using double-layer rectangular windings, as illustrated in Figure 5. The primary coil consists of $2 \times 11$ turns with dimensions of 450 mm $\times$ 150 mm, while the secondary coil comprises $2 \times 10$ turns with dimensions of 400 mm $\times$ 100 mm. The vertical air gap between the coils is maintained at 85 mm. Ferrite sheets of 4 mm thickness and aluminium shielding of 2 mm thickness are incorporated beneath the windings to guide the magnetic flux and limit stray fields, as shown in the different views of Figure 5.

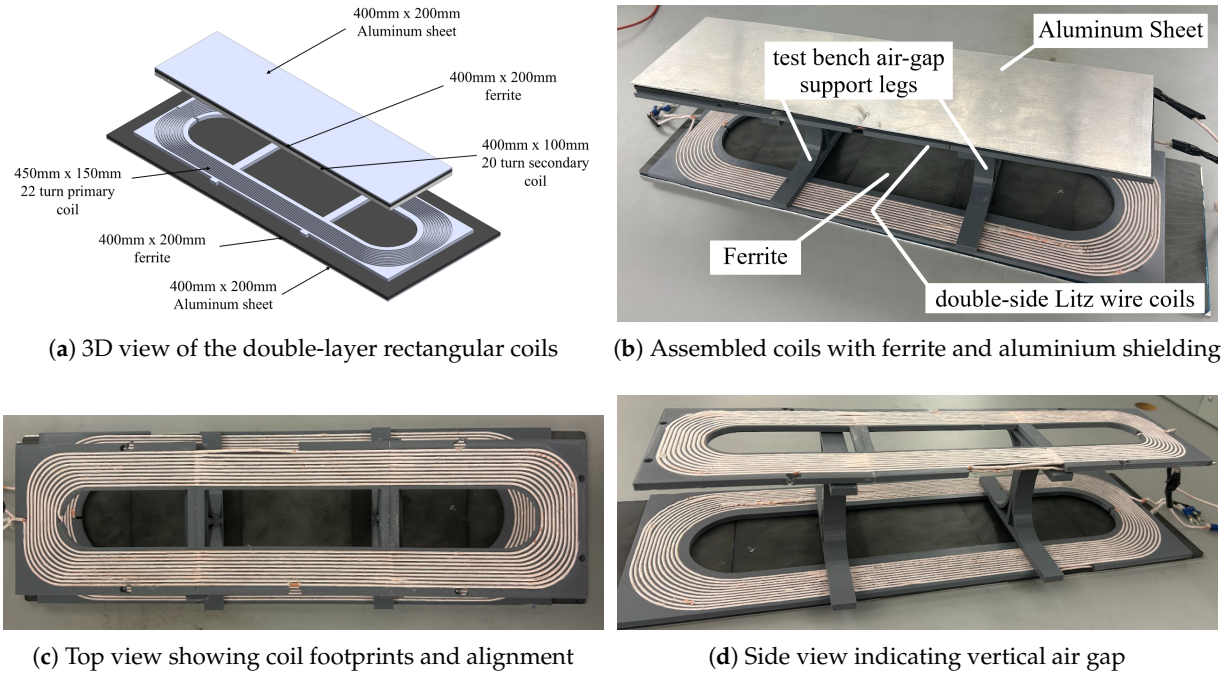
The primary and secondary coils are characterized by their self-inductances $L_p$ and $L_s$, and their internal resistances $R_p$ and $R_s$, respectively. The interaction between the coils is governed by the coupling coefficient $k$, which depends on their physical alignment and separation. The corresponding mutual inductance $M$ defines how effectively energy is transferred from the primary to the secondary side and is represented as:

$$M = k\sqrt{L_p L_s}. \tag{3}$$

To improve power transfer efficiency and establish resonant operation, SS compensation topology is employed. Capacitors $C_p$ and $C_s$ are connected in series with the primary and secondary coils, respectively. These capacitors are selected such that the system operates at resonance when the inverter switching frequency matches the resonant frequency based on the parameters mentioned in Table 1. The corresponding switching angular frequency $\omega$ is given by:

$$\omega = \frac{1}{\sqrt{L_p C_p}} = \frac{1}{\sqrt{L_s C_s}}. \tag{4}$$

At resonance, the reactive effects of inductance and capacitance cancel out, resulting in approximately sinusoidal currents in both coils and enhanced power transfer capability.




(**a**) 3D view of the double-layer rectangular coils

(**b**) Assembled coils with ferrite and aluminium shielding

(**c**) Top view showing coil footprints and alignment

(**d**) Side view indicating vertical air gap

**Figure 5.** Coil assembly for the WPT interface: (**a**) 3D view of the double-layer rectangular windings; (**b**) assembled coils with ferrite sheets and aluminium shielding; (**c**) top view showing pad dimensions and relative alignment; (**d**) side view highlighting the 85 mm air gap.

### *2.4. Rectifier and Equivalent Load Representation*

On the secondary side, the induced voltage across the receiving coil is denoted as $v_s$, which drives the secondary current $i_s$. This high-frequency *ac* voltage is converted into *dc* by a full-bridge rectifier composed of diodes $D_1$–$D_4$. A filter capacitor $C_o$ is used to smooth the rectified voltage, producing a stable *dc* output. The voltage $v_s$ at the rectifier input is a square waveform. Using Fourier series expansion, this waveform can be expressed as a sum of harmonic components, as given below:

$$v_s(t) = \sum_{n=1,3,5,\ldots}^{\infty} \frac{4V_o}{n\pi} \sin(n\omega t). \tag{5}$$

The RMS value of the fundamental component of $v_s$ by FHA is given by:

$$V_{s,\mathrm{rms}} = \frac{2\sqrt{2}}{\pi} V_o. \tag{6}$$

For analytical purposes, the rectifier–load combination is often represented by an equivalent resistance $R_e$. This equivalent resistance can be related to the output load resistance $R_o$ as:

$$R_e = \frac{8}{\pi^2} R_o. \tag{7}$$

### *2.5. Equivalent Circuit Modeling and Analysis*

Using the FHA, the WPT system can be described by an equivalent mutual inductance model shown in Figure 6 which is further transformed into the T-equivalent representation. In the T-equivalent circuit, the coupled coils are expressed as an uncoupled inductance on each side together with an intermediate branch that reflects the mutual coupling. This representation is particularly convenient for applying Kirchhoff's voltage law (KVL) and deriving expressions for the resonant currents and voltages in the WPT system.

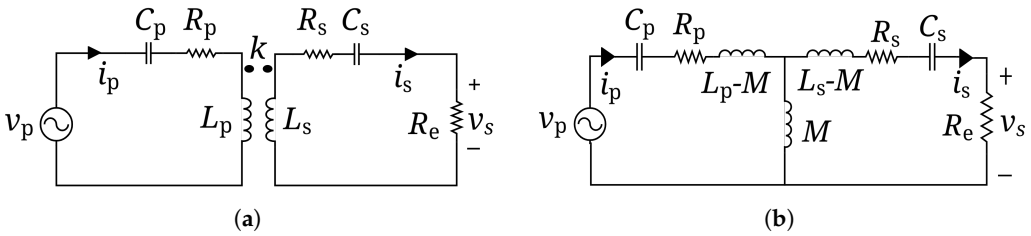



**Figure 6.** Equivalent circuit representations of the WPT system: (**a**) mutual inductance model and (**b**) T-model.

By applying KVL to the T-equivalent circuit, a set of coupled equations that describe the relationship between the voltages and currents in the system are obtained:

$$\vec{v}_p = Z_p \vec{i}_p - j\omega M \vec{i}_s, \tag{8}$$

$$\vec{v}_s = -Z_s \vec{i}_s + j\omega M \vec{i}_p, \tag{9}$$

where $Z_p$ and $Z_s$ denote the primary and secondary-side impedances respectively, and are given by:

$$Z_p = R_p + j\omega L_p + \frac{1}{j\omega C_p}, \qquad Z_s = R_s + j\omega L_s + \frac{1}{j\omega C_s}. \tag{10}$$

$\vec{v}_s$ in Equation (9) can also be written as:

$$\vec{v}_s = R_e \vec{i}_s. \tag{11}$$

Substituting (11) into (9) yields:

$$(R_e + Z_s)\vec{i}_s = j\omega M \vec{i}_p. \tag{12}$$

Equations (8) and (12) can then be solved simultaneously to obtain expressions for the primary and secondary currents as functions of $\vec{v}_p$:

$$\vec{i}_p = \frac{(Z_s + R_e)}{Z_p(Z_s + R_e) + \omega^2 M^2} \vec{v}_p, \tag{13}$$

$$\vec{i}_s = \frac{j\omega M}{Z_p(Z_s + R_e) + \omega^2 M^2} \vec{v}_p. \tag{14}$$

These expressions for $\vec{i}_p$ and $\vec{i}_s$ are important for analyzing the resonant behavior of the system and for evaluating the power transfer characteristics under different coupling and load conditions.

The current flowing through the load corresponds to the average value of the rectified secondary-side current. Considering only the fundamental component of the secondary current, with peak value $I_{s1}$, $I_o$ can be written as:

$$I_o = \frac{1}{\pi}\int_0^{\pi} I_{s1}\sin\theta\, d\theta = \frac{2I_{s1}}{\pi}. \tag{15}$$

Using the previously derived expressions for the fundamental secondary current and the equivalent load, the expressions for $I_o$ and $V_o$ can be obtained as:

$$I_o = \frac{8\omega M V_{dc}}{\pi^2 Z_p Z_s + 8Z_p R_o + \pi^2\omega^2 M^2}\cos\left(\frac{\varphi}{2}\right), \tag{16}$$

$$V_o = \frac{8\omega M R_o V_{dc}}{\pi^2 Z_p Z_s + 8Z_p R_o + \pi^2\omega^2 M^2}\cos\left(\frac{\varphi}{2}\right). \tag{17}$$

Equations (16) and (17) clearly show that $I_o$ and $V_o$ depend on the phase shift, the load resistance, the input *dc* voltage, and the coupling and resonant parameters of the WPT system.

## 3. Load Estimation

Primary-side control schemes in WPT systems are often implemented using secondary-side feedback conveyed through a wireless communication channel. Although this approach provides accurate information about the load and operating conditions on the vehicle side, it also introduces practical challenges such as transmission delay, packet loss, reduced reliability, and increased implementation complexity. In addition, the communication link may be intermittently unavailable due to environmental interference, coil misalignment, or unexpected link failures, which can compromise the continuity of the charging process. From a system-security perspective, the communication channel may also be exposed to cyber threats, including data interception or manipulation, motivating a reduction in dependence on exchanged secondary-side signals. Therefore, in this work, the control strategy is designed to operate without direct wireless feedback from the secondary side; instead, the required information is inferred from primary-side electrical quantities.

To enable such primary-side estimation, the input impedance $Z_{\text{in}}$ of the WPT system, as seen from the primary side, is first obtained from the mutual inductance model as [23]:

$$\begin{aligned} Z_{\text{in}} = {} & R_p + j\omega L_p - j\frac{1}{\omega C_p} + \frac{\omega^2 M^2}{R_e + R_s + j\omega L_s - j\frac{1}{\omega C_s}}\left[R_p + \frac{\omega^2 M^2 (R_e + R_s)}{(R_e + R_s)^2 + \left(\omega L_s - \frac{1}{\omega C_s}\right)^2}\right] \\ & + j\left[\omega L_p - \frac{1}{\omega C_p} - \frac{\omega^2 M^2\left(\omega L_s - \frac{1}{\omega C_s}\right)}{(R_e + R_s)^2 + \left(\omega L_s - \frac{1}{\omega C_s}\right)^2}\right]. \end{aligned} \tag{18}$$

The active input power $P_1$ at the primary side can then be expressed in terms of the real part of $Z_{\text{in}}$ and the primary RMS current $I_{p,\text{rms}}$ as:

$$P_1 = I_{p,\text{rms}}^2 \, \Re\{Z_{\text{in}}\} = I_{p,\text{rms}}^2 \left[ R_p + \frac{\omega^2 M^2 (R_e + R_s)}{(R_e + R_s)^2 + \left(\omega L_s - \frac{1}{\omega C_s}\right)^2} \right]. \tag{19}$$

When the system operates at the tuned resonant frequency, the imaginary part of the input impedance becomes zero, which simplifies the relationship between $P_1$, $I_{p,\text{rms}}$ and $R_e$. Since, $R_o$ can be related to $R_e$ by Equation (7), it can be estimated from primary-side measurements as:

$$R_o = \frac{\pi^2}{8} \left[ \frac{\omega^2 M^2 I_{p,\text{rms}}^2}{P_1 - R_p I_{p,\text{rms}}^2} - R_s \right]. \tag{20}$$

In the context of LEV battery charging, $R_o$ is not directly accessible from the primary side and varies during the charging process with battery state-of-charge (SOC) and operating conditions. By estimating $R_o$ from $P_1$ and $I_{p,\text{rms}}$, the controller obtains an indirect but reliable representation of the actual load.

## 4. Battery Simulator Setup

A battery simulator model is employed to emulate realistic voltage response of a battery for a given current load profile.

Other inputs to the battery simulator include the parameters of its open circuit voltage (OCV) to state of charge (SOC) characteristics and its relaxation effect; both of these parameters are dependent on the battery chemistry. For NMC batteries, the OCV-SOC characteristics is quite steep and its time constant (the relaxation parameter) is shorter; in contrast, for LFP batteries the OCV-SOC curve is quite flat in the mid region and the time constant is comparatively long.

The experimental OCV-SOC parameters used in this work are obtained by characterizing a cylindrical NMC cell (see [24] for details). The OCV-SOC curve is parameterized according to the combined+3 model as follows

$$V_\circ(s) = k_0 + \frac{k_1}{s} + \frac{k_2}{s^2} + \frac{k_3}{s^3} + \frac{k_4}{s^4} + k_5 s + k_6 \ln(s) + k_7 \ln(1 - s) \tag{21}$$

where $V_\circ(s)$ denotes the OCV, $s$ denotes the SOC, and $k_0 = -9.082$, $k_1 = 103.087$, $k_2 = -18.185$, $k_3 = 2.062$, $k_4 = -0.102$, $k_5 = -76.604$, $k_6 = 141.199$, and $k_7 = -1.117$. These parameters need to be used with scaling [25] with the linear symmetrical scaling factor of $\epsilon = 0.175$. The parameters of the cell are then scaled to a pack that had 13 cells in series and 4 cells in parallel. The resulting battery pack model approximates the required battery pack model that had a minimum voltage of 36.4 V, maximum voltage of 54.6 V, and nominal capacity of 12 Ah. The relaxation parameters of the battery cell are selected to represent typical time constant of a battery cell of comparable size $R_0 = 0.1\ \Omega$, $R_1 = 0.05\ \Omega$, $R_2 = 0.02\ \Omega$, $C_1 = 500$ F and $C_2 = 1000$ F and are scaled using the pack configuration of 13S4P. Here, $R_0$ is the series resistance of the cell and $R_1, C_1$ and $R_2, C_2$ are the parameters of the first and second RC components of the battery equivalent circuit model that is used to model the relaxation effect of the battery cell in Figure 7. Finally, the standard deviation of the measurement noise levels for current and voltage are defined as $\sigma_i = 0.1$ mA and $\sigma_v = 0.1$ mV, respectively. More details of the battery simulator, including MATLAB R2025a codes can be found with details in [26].

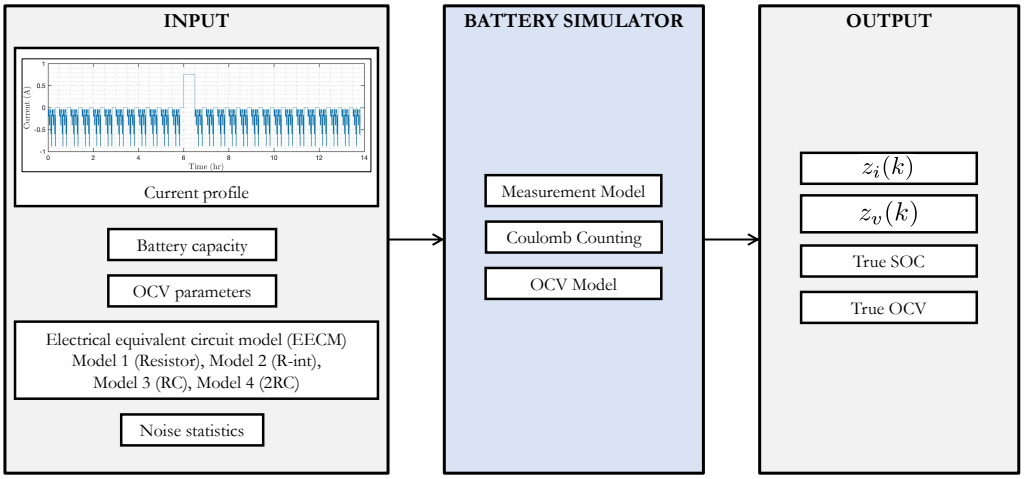



**Figure 7.** Battery Simulator with input and output for experimental OCV-SOC parameters.

## 5. MPC Control Framework

MPC is an optimization-based strategy that uses a mathematical model of the plant to predict the effect of candidate control inputs and select the one that minimizes a cost function. It is particularly attractive for power electronic converters and WPT systems, which exhibit pronounced nonlinear behaviour and wide operating ranges that are not easily handled by conventional linear control schemes. In such applications, MPC can deliver rapid transient response, manage multivariable and coupled dynamics in a systematic way, and balance objectives such as tracking accuracy, efficiency, and constraint satisfaction within a single optimization framework [27].

MPC strategies are commonly grouped into two main classes: finite-control-set MPC (FCS-MPC) and continuous-control-set MPC (CCS-MPC). In FCS-MPC, the controller works directly with a discrete set of switch states, predicting the resulting currents and voltages for each candidate state and choosing the one that yields the minimum cost. This direct manipulation of switching states removes the need for a separate modulator but typically produces a switching pattern with variable frequency. In contrast, CCS-MPC treats the control input as a continuous signal, such as duty cycle or phase-shift angle. The resulting continuous signal is then translated into gate pulses by a conventional modulation stage, so the switching frequency is imposed by the modulator and remains constant. This arrangement preserves the model-based optimization capabilities of MPC while maintaining a fixed switching frequency that aligns with practical design targets and regulatory limits [22].

In the proposed SS-compensated WPT system for LEV charging, a MPC framework shown in Figure 8 is adopted to satisfy the fixed resonant-frequency constraint imposed by the compensation network and WPT standards. The phase-shift angle of the primary full-bridge inverter is chosen as the continuous control variable, while a phase-shift modulator maintains constant switching frequency at the designed resonant value. At each sampling instant, the controller computes the phase-shift command that minimizes a current-tracking cost function, thus achieving accurate current regulation without disturbing the tuned resonant operation.

In CCS-MPC, a general quadratic cost function can be written as:

$$J(N_s, N_p, N_c) = \sum_{i=N_s}^{N_p} \Lambda(i) \left[ z(k+i) - r(k+i) \right]^2 + \sum_{i=1}^{N_c} \Gamma(i) \left[ \Delta v(k+i) \right]^2, \quad (22)$$

where $N_s$ is the model delay index, $N_p$ is the prediction horizon, and $N_c$ is the control horizon. The terms $z(k)$ and $r(k)$ denote the predicted output and its reference, $\Delta v$ represents the control signal, and $\Lambda(i)$ and $\Gamma(i)$ are non-negative weighting factors that determine the relative importance of tracking accuracy and control effort in the optimization.

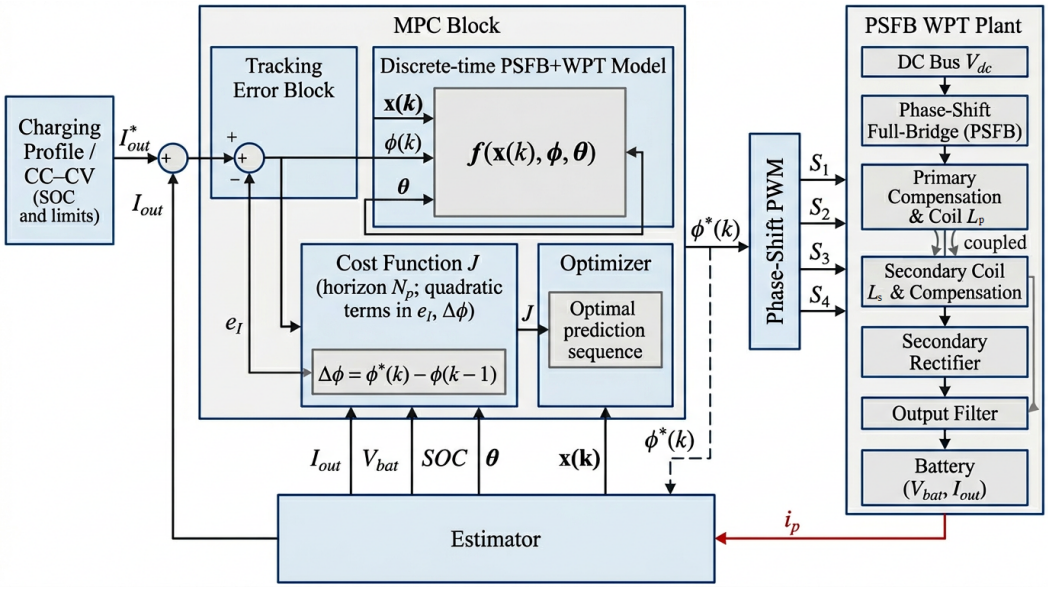



**Figure 8.** Control structure of the proposed MPC-based wireless power transfer with embedded battery model and phase-shift optimization.

In the proposed controller, the objective is restricted to fast tracking of a single output variable without explicit penalization of control moves or additional constraints. Accordingly, the control-effort term is omitted by setting $\Gamma(i) = 0$. The prediction horizon is limited to one step ($N_p = 1$) in order to keep the computational burden low, which is sufficient for voltage and current tracking in power electronic applications [28]. The model delay index is chosen as $N_s = 1$ and the corresponding output weighting factor is set to unity, $\Lambda(i) = 1$, so that only the immediate tracking error of the predicted output contributes to the cost.

Under these assumptions, (22) simplifies to a single-step tracking cost:

$$J = \big(z(k+1) - r(k+1)\big)^2. \tag{23}$$

In the present WPT application, $z$ corresponds to $I_o$ obtained from the analytical SS-compensated converter model as a function of $\varphi$, and $r$ is the current reference $I_{\mathrm{ref}}$. Therefore, the cost function used in the controller can be written explicitly as:

$$J(\varphi) = \big(I_o(\varphi) - I_{\mathrm{ref}}\big)^2, \tag{24}$$

which directly penalizes the squared deviation between the predicted steady-state load current and its desired value for each candidate phase-shift angle $\varphi$.

Figure 8 illustrates the overall control structure of the proposed MPC-based current controller. In each sampling interval, $V_{p,\mathrm{rms}}$ and $I_{p,\mathrm{rms}}$, are measured and used to compute $P_1$, which is then employed to estimate $R_o$ according to (20). Together with $V_{\mathrm{dc}}$, the estimated $R_o$ is then passed to the steady-state model of the SS-compensated WPT converter. Using this model, the controller calculates the corresponding predicted steady-state output currents $I_o(\varphi)$ for a finite set of candidate phase-shift angles $\varphi \in [0, \pi)$ . For each candidate, the current-tracking cost is computed according to (24). The phase-shift value that yields the minimum cost is selected as the optimal command $\varphi^*$ and applied to

the phase-shift modulation block, which generates the full-bridge gating signals at fixed switching frequency.

From a closed-loop perspective, the proposed single-step CCS-MPC acts as a nonlinear feedback policy that selects the phase-shift command $\phi^*(k)$ which minimizes the instantaneous current-tracking cost $J = (I_o(\phi, k) - I_{\text{ref}})^2$ at each sampling instant. Although a full Lyapunov-based proof is beyond the scope of this work, the steady-state analytical model in (16) and (17) implies that, within the operating range of interest, the mapping $\varphi \mapsto I_o(\varphi)$ is continuous and strictly monotonic for fixed load and coupling conditions. Under this monotonicity and with $\varphi$ constrained to a compact interval, the minimization of $J$ yields a unique optimal phase shift that drives the tracking error $I_o - I_{\text{ref}}$ toward zero. Moreover, the battery SOC and coupling coefficient vary slowly compared to the control update rate, so the closed-loop behaviour can be interpreted as a contractive iteration around the operating point.

## 6. Simulation Methodology

The proposed control strategy is first evaluated in a detailed time-domain simulation environment, whose overall structure is shown in Figure 9. The complete model is implemented in MATLAB/Simulink and comprises the PSFB *dc-dc* converter. Load-$R_o$ estimation is implemented using a MATLAB Function block with a second MATLAB Function block that performs steady-state output-current prediction, cost-function evaluation, and optimal phase-shift selection. PWM pulses are generated using another MATLAB Function block that produces phase-shifted gating signals at a fixed switching frequency.

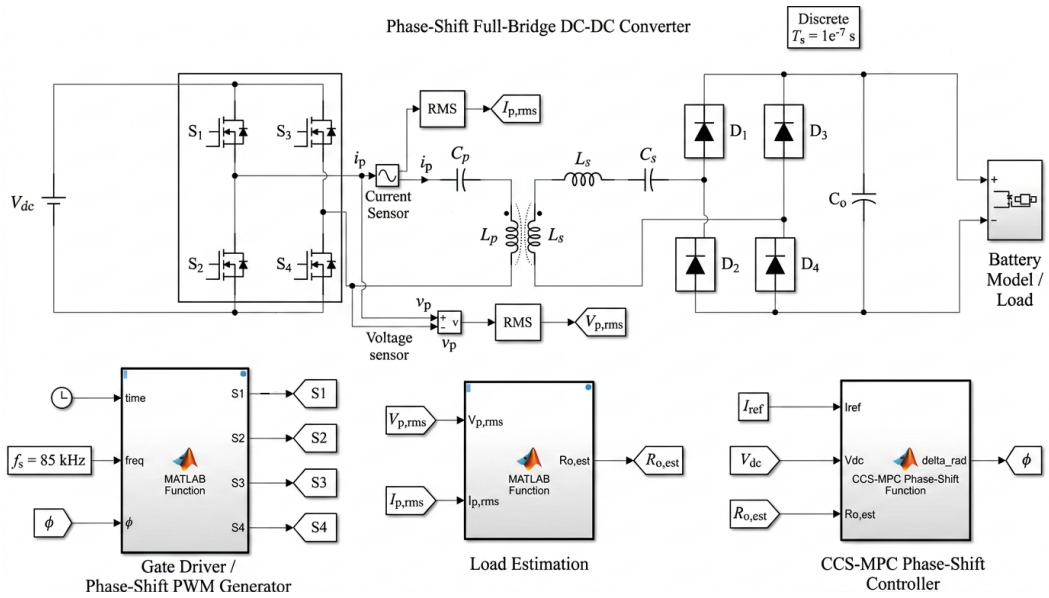



**Figure 9.** MATLAB/Simulink model of the phase-shifted full-bridge (PSFB) converter.

The electrical parameters used in the simulations are summarized in Table 1. The WPT link model includes the primary and secondary coil inductances, resonant capacitors, mutual inductance, and coupling coefficient corresponding to the nominal air-gap distance and alignment conditions. To capture realistic converter behavior, the primary full-bridge MOSFETs are modeled as non-ideal devices, with on-state resistance, body-diode conduction, parasitic output capacitance, and finite rise and fall times specified in Table 2. It is necessary to assess the impact of switching dynamics and device non-idealities on current-control performance and soft-switching behavior.

**Table 1.** System parameters of the WPT setup.

| Parameter | Value |
|---|---|
| Rated output power | 100 W |
| Switching frequency | 85 kHz |
| Primary coil inductance ($L_1$) | 406 µH |
| Primary coil resistance | 807 mΩ |
| Primary compensation capacitor | 8 nF |
| Coupling coefficient ($k$) | 0.1208 |
| Secondary coil inductance ($L_2$) | 218 µH |
| Secondary coil resistance | 503 mΩ |
| Secondary compensation capacitor | 16 nF |
| Air gap distance | 85 mm |

**Table 2.** MOSFET device parameters.

| Parameter | Value |
|---|---|
| On-state resistance ($R_{DS(on)}$) | 30 mΩ |
| Rise time ($t_r$) | 9 ns |
| Fall time ($t_f$) | 18 ns |
| Output capacitance ($C_{oss}$) | 176 pF |
| Body-diode forward voltage ($V_f$) | 2.7 V |

Using this setup, the MPC controller is tested over different battery operating points. Figure 10 shows representative simulated waveforms at a low SOC operating point of 20% with $I_{\text{ref}} = 1$ A. The top-left and bottom-left waveforms show the corresponding phase-shift between $S_1$ and $S_4$ switches while delivering $v_p, i_p$ and $v_s, i_s$. The top-right and bottom-right shows the output $V_o, I_o$. These results verify that the MPC controller can accurately track $I_{ref}$, preserve the desired soft-switching conditions, and maintain stable operation at the rated power level under nominal coupling conditions.

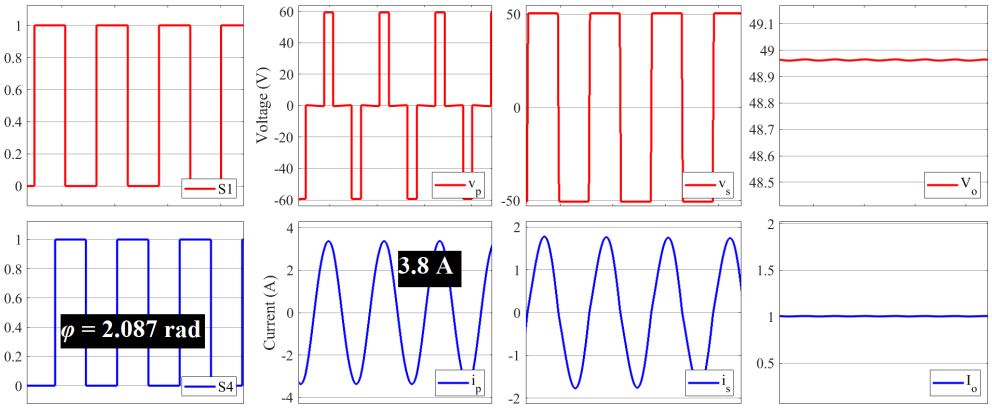
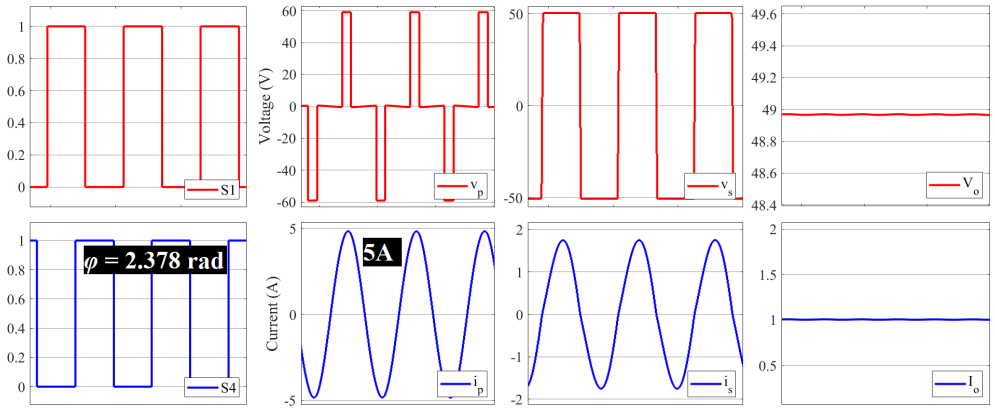



**Figure 10.** Waveforms of the PSFB-based WPT system at 20% SOC, showing gate signals ($S_1$, $S_4$), primary and secondary voltages, primary and secondary currents, and output voltage and current responses under constant-current charging operation.

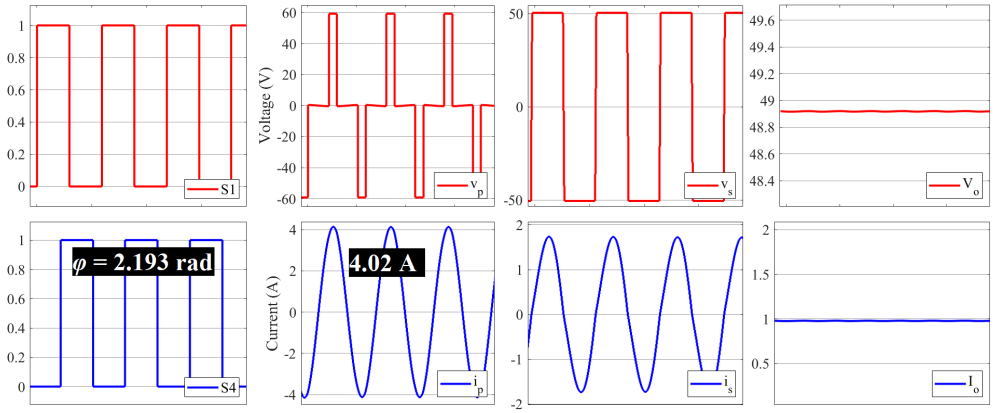
### *6.1. Misalignment Conditions in Simulations*

To evaluate robustness, coil misalignment is introduced in the simulation model through lateral and angular offsets between the primary and secondary coils parameters, emulating practical LEV-to-station positioning errors. Controller performance under misalignment is evaluated at a battery SOC of 20% with $I_{\text{ref}} = 1$ A. Figure 11 shows the

simulated waveforms for lateral and angular misalignment. The results confirm that the CCS-MPC maintains stable operation and accurately tracks the commanded current in both scenarios, with limited overshoot and short settling time. However, angular misalignment produces comparatively higher transient spikes due to the more pronounced reduction in coupling coefficient and mutual inductance, resulting in a sharper degradation in power-transfer capability.




(**a**) Lateral misalignment at 20% SOC




(**b**) Angular misalignment at 20% SOC

**Figure 11.** Waveforms of the PSFB-based WPT system under (**a**) lateral and (**b**) angular misalignment at 20% SOC, showing gate signals, primary and secondary voltages, primary and secondary currents, and output voltage and current responses under constant-current charging operation.

The corresponding parameter variations for aligned and misaligned cases are summarized in Table 3. These values are derived from measured inductance data and are used consistently in both simulation and hardware studies.

**Table 3.** Coil parameters under different alignment conditions.

| Parameter | Lateral | Angular | Aligned |
|---|---|---|---|
| $L_p$ (µH) | 408 | 407 | 406 |
| $L_p$ ($L_s$ shorted) (µH) | 405 | 403 | 400 |
| $L_s$ (µH) | 220 | 219 | 218 |
| $L_s$ ($L_p$ shorted) (µH) | 218 | 217 | 216 |
| Coupling coefficient ($k$) | 0.0857 | 0.0991 | 0.1216 |
| Mutual inductance (µH) | 25.69 | 29.60 | 36.17 |

### *6.2. Experimental Validation*

The proposed WPT system and MPC control strategy are experimentally validated on a laboratory prototype designed to operate under CC charging conditions. The primary-side *dc* input is provided by a programmable *dc* source rated for 0–100 V, 0–5 A, and 500 W, which ensures a well-regulated input voltage with integrated protection during testing. The primary full-bridge inverter is realized using two EVLSTGAP3SXS-H half-bridge evaluation boards populated with SCTWA70N120G2V-4 SiC MOSFETs (1200 V, 91 A, 30 mΩ) and isolated STGAP3SXS gate drivers shown in circled part of Figure 12. On the secondary side, a full-bridge Schottky rectifier (600 V, 10 A) followed by an output filter capacitor interfaces the WPT link to a 48 V, 10 Ah lithium-ion battery pack. The compensation network, coils, and air-gap are implemented to match the parameters used in Table 1, ensuring that the experimental platform closely reflects the simulated system.

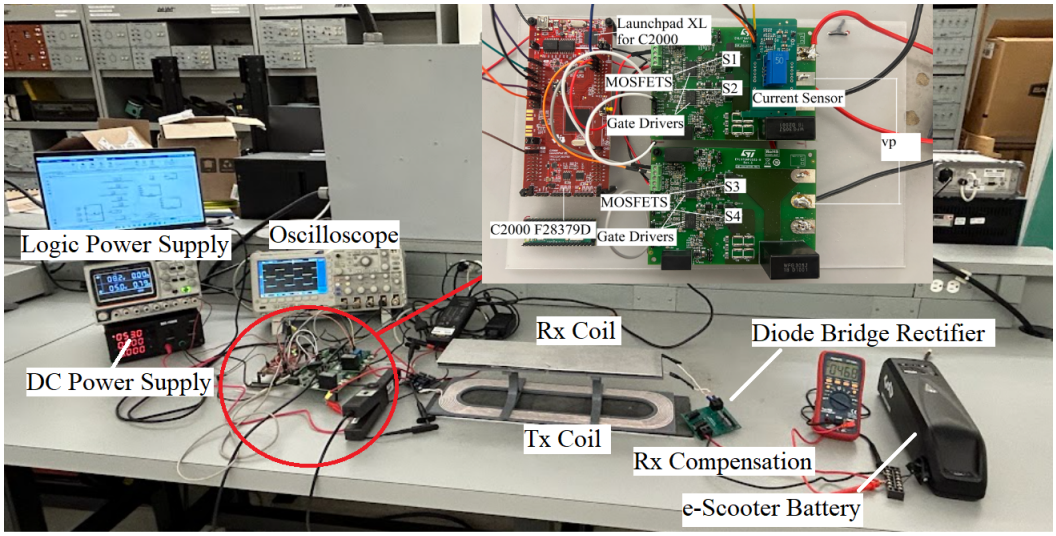



**Figure 12.** Experimental validation of the proposed MPC-based WPT system, comprising the complete hardware setup including power stage, compensation network, control platform, and measurement instrumentation.

### *6.3. Control Implementation*

The MPC algorithm is implemented on a C2000 microcontroller (Texas Instruments, Dallas, TX, USA), which is responsible for real-time control execution and PWM generation. As depicted in Figure 13, the MCU acquires $I_{ref}$ and $i_p$, performs an online $R_o$ estimation, predicts the steady-state output $I_o$ for current phase-shift ($\varphi$) values, computes the cost function, and selects the optimal phase-shift ($\varphi^*$) within each sampling interval. The selected phase shift is then applied to the full-bridge inverter through high-resolution PWM modules synchronized to the fixed switching frequency with 150 ns dead-time. There is no electrical feedback or wireless communication from the secondary side. In addition, the MCU supervises primary-side current and the estimated reflected load, and triggers a rapid phase-shift ramp-down and bridge shutdown when over-current or receiver-removal conditions are detected, preventing excessive resonant currents in the S–S compensated tank.

To guarantee real-time feasibility, the control scheme is optimized to minimize computational overhead and memory usage, with all critical computations scheduled within a single PWM period. The resulting CPU utilization and execution-time margins are later quantified, confirming that the proposed MPC implementation satisfies the timing constraints of the embedded platform without compromising control performance.

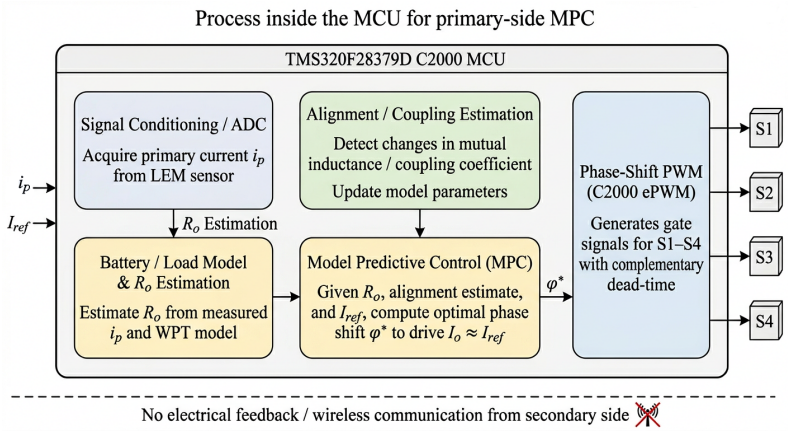



**Figure 13.** Control execution flow of the MPC algorithm inside the C2000 microcontroller for primary-side WPT control.

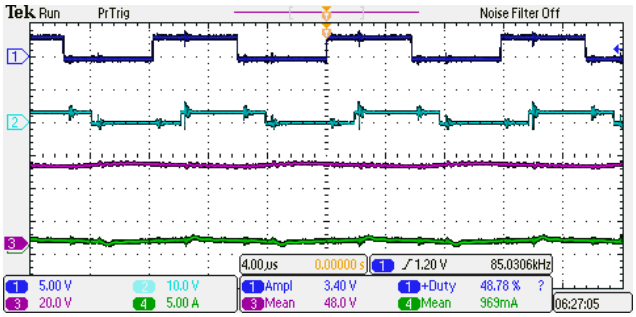
## 7. Results and Discussion

The experimental results validate the effectiveness of the proposed MPC strategy for wireless charging of LEV under practical operating conditions, including varying battery SOC, coil misalignment, and embedded implementation constraints.

### *7.1. Steady-State Charging Performance*

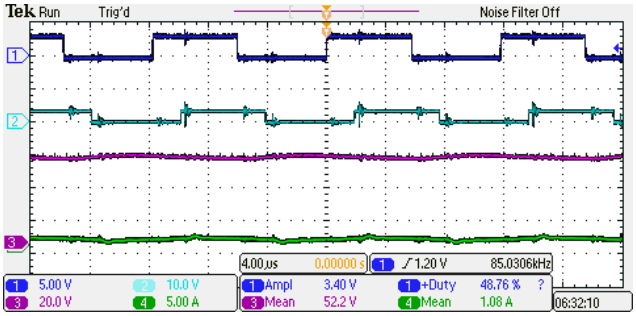
The steady-state operation of the system is demonstrated in Figure 14, which correspond to low and high SOC conditions, respectively. At 20% low SOC, the controller regulates the battery current in CC mode, maintaining a stable charging current that matches the $I_{ref}$ while preserving the desired soft-switching behavior of the converter. At 75% high SOC, the system naturally transitions toward a higher voltage predicted by battery characteristics.

In both cases, the phase-shift is smoothly adjusted by MPC, confirming that the predictive model successfully captures the nonlinear battery dynamics and the dependence of power transfer on operating conditions. As a result, the output current trajectory exhibits low ripple and negligible steady-state error, without the trial-and-error tuning or integral action typically required by conventional feedback controllers. This behavior is particularly advantageous for battery charging, where minimizing current ripple and avoiding abrupt changes in charging conditions can contribute to reduced thermal and electrochemical stress.




(**a**) 20% SOC (48.4 V)

**Figure 14.** *Cont.*




(**b**) 75% SOC (52.2 V)

**Figure 14.** Oscilloscope waveforms of the PSFB-based WPT system showing gate signals ($S_1$, $S_4$), phase-shift control, and corresponding output voltage and current under different SOC conditions.

### *7.2. Dynamic Response Under Misalignment*

To substantiate the robustness of the MPC scheme under realistic operating disturbances, controlled misalignment tests are performed on the experimental setup. Lateral and angular misalignment cases are introduced by physically displacing and tilting the receiver coil $R_x$ relative to the transmitter coil $T_x$, as illustrated in Figure 15 for the scooter platform and in Figure 16 for the corresponding coils on lab test bench. These test conditions are selected to reflect typical misplacement scenarios encountered in LEV charging, where precise coil alignment cannot always be ensured in practice.

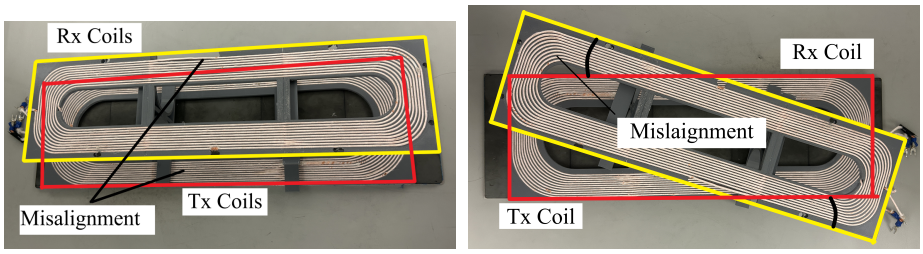


(**a**) Scooter misaligned (lateral) (**b**) Scooter misaligned (angular)

**Figure 15.** Scooter misalignment cases: (**a**) lateral misalignment; (**b**) angular misalignment.

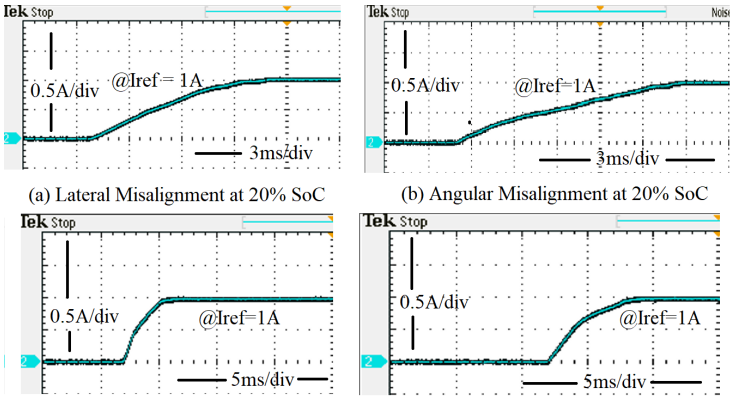
The misalignment magnitudes and directions are chosen to match the parameter variations summarized in Table 3, thereby aligning the experimental test cases with the simulated coil-parameter sets. During each test, the system operates at a fixed $I_{ref}$ and battery SOC, while the resulting convergence behavior, steady-state current, and inverter phase-shift command are recorded for analysis. These measurements form the basis of the misalignment-robustness results discussed in Results and Discussion, where the MPC performance is quantitatively compared to other popular controllers. The corresponding convergence characteristics of the MPC controller under these conditions are summarized in Figure 17.

The results show that misalignment directly degrades the coupling coefficient and mutual inductance, leading to a reduction in power-transfer capability and a change in the effective dynamics of the resonant tank. Despite these perturbations, the MPC maintains a consistent and rapid convergence to the desired reference current across the tested SOC and alignment conditions. Lateral misalignment leads to a gradual reduction in coupling and a moderate increase in convergence time, whereas angular misalignment causes more abrupt changes in flux linkage and manifests as sharper deviations in the initial transient. In both scenarios, the controller converges to the reference current without excessive overshoot or sustained oscillations.




(**a**) Lateral misalignment in coils (**b**) Angular misalignment in coils

**Figure 16.** Coil misalignment cases: (**a**) lateral misalignment; (**b**) angular misalignment.



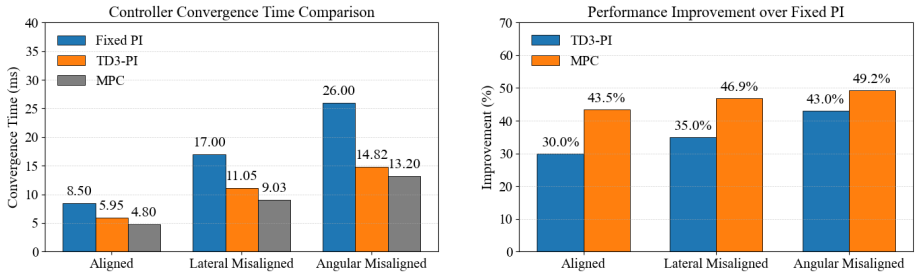

(a) Lateral Misalignment at 20% SoC (b) Angular Misalignment at 20% SoC

(c) Aligned (20% SoC) (d) Aligned (75% SoC)

**Figure 17.** $I_{\text{out}}$ for the MPC-WPT system under different operating conditions at $I_{\text{ref}} = 1$ A showing variations in convergence speed and transient response.

### *7.3. Comparison with Conventional and Learning-Based Controllers*

A quantitative comparison between the proposed MPC, a Fixed-gain PI controller, and a TD3-PI controller is presented in Figure 18 [21]. Figure 18a reports the convergence time for all controllers under aligned, lateral-misalignment, and angular-misalignment conditions, while Figure 18b highlights the percentage improvement of the MPC and TD3-PI controllers relative to the Fixed PI baseline.




(**a**) Convergence time comparison of all controllers (**b**) Performance improvement over Fixed PI

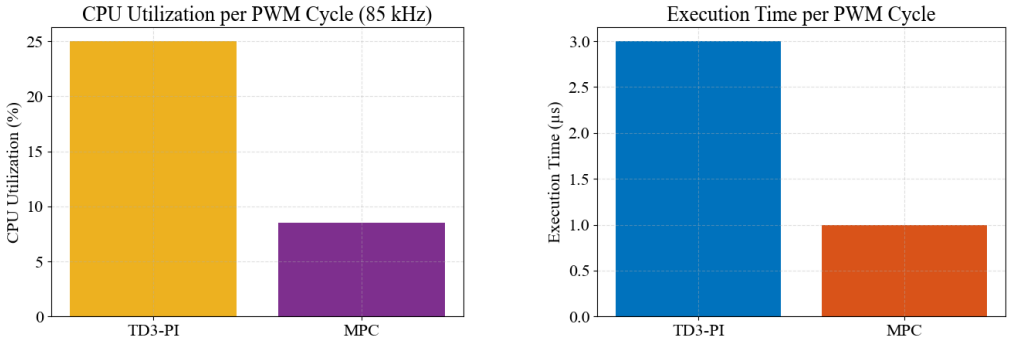
**Figure 18.** Comparison of control strategies under aligned and misaligned conditions: (**a**) convergence time comparison and (**b**) percentage improvement over Fixed PI.

Across all operating points, the MPC achieves the fastest convergence to the $I_{ref}$, with the least sensitivity to alignment and SOC variations. This improvement stems from the direct computation of the optimal $\varphi^*$ at each sampling instant, eliminating the cumulative delays and gain-scheduling limitations inherent to feedback loops. The Fixed PI controller exhibits slower response and increased overshoot, particularly under misalignment, due to the mismatch between tuned gains and the varying plant dynamics.

The TD3-PI controller improves adaptability and reduces convergence time relative to Fixed PI, but still slower than MPC and introduces additional computational overhead and convergence latency associated with policy evaluation.

### *7.4. Computational Efficiency and Real-Time Feasibility*

The real-time feasibility of the control strategies is evaluated through CPU-utilization and execution-time measurements on the C2000 MCU, as shown in Figure 19. Figure 19a reports the CPU utilization per PWM cycle for the CCS-MPC and TD3-PI implementations, while Figure 19b shows the corresponding execution time per PWM period.

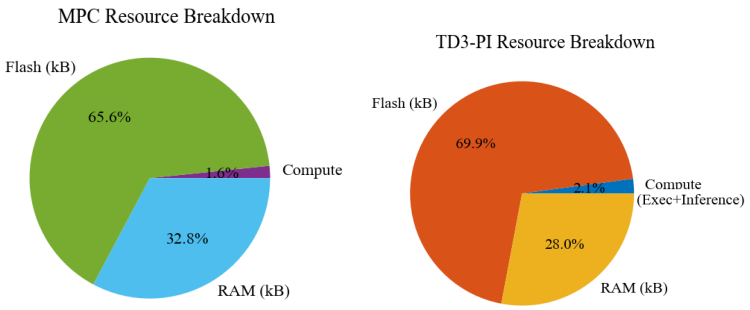



(**a**) (**b**)

**Figure 19.** Performance comparison of control implementations: (**a**) CPU utilization per PWM cycle and (**b**) execution time per PWM cycle.

The results indicate that the MPC implementation achieves lower CPU utilization and shorter execution times compared to the TD3-PI controller, while still providing superior dynamic performance. This behavior can be attributed to the deterministic, model-based nature of MPC, which relies on closed-form predictions and compact cost-function evaluation, as opposed to the repeated policy inference required by the learning-based approach. The measured execution times remain comfortably below the available PWM period, confirming that the MPC can be deployed on resource-constrained embedded platforms without violating timing constraints.

The resource-utilization breakdown in Figure 20 further supports this conclusion. The MPC controller exhibits a smaller memory footprint and reduced reliance on large parameter sets, whereas the DRL TD3-PI implementation requires additional resources for storing and processing learning-based control parameters. This distinction is particularly important for automotive-grade embedded systems, where cost, power consumption, and computational efficiency are critical design constraints.




(**a**) MPC resource breakdown (**b**) TD3-PI resource breakdown

**Figure 20.** Resource utilization comparison: (**a**) MPC controller and (**b**) TD3-PI controller showing computational and memory breakdown.

### *7.5. Control Smoothness and Battery Stress Reduction*

The impact of control strategy on charging smoothness is illustrated in Figure 21, which shows the variation of phase shift across the full SOC range in simulation using the high-fidelity battery model. The MPC produces a smooth and nearly monotonic phase-shift trajectory as the battery voltage evolves, reflecting its predictive nature and coordinated control action.

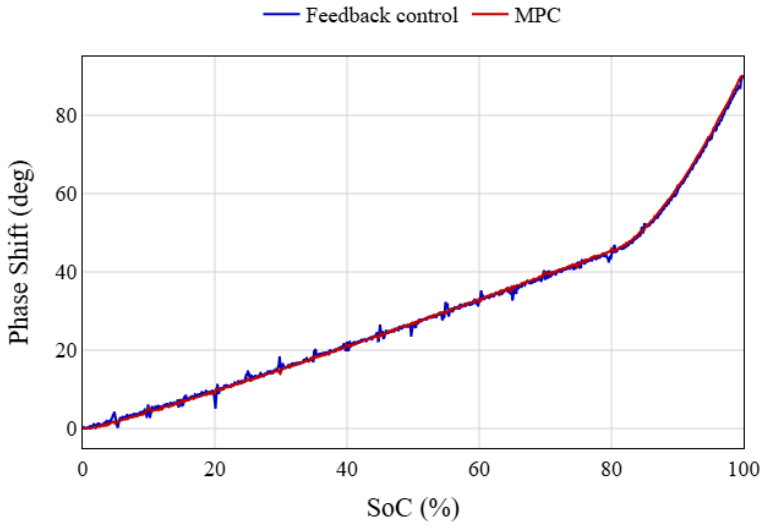



**Figure 21.** Optimal Phase shift variations comparison in WPT simulations between proposed MPC and Feedback control.

In contrast, the feedback-based controller exhibits noticeable fluctuations due to continuous error correction, particularly in regions where system dynamics vary rapidly. These differences directly translate into the battery-current waveforms shown in Figure 22. obtained from the same simulated CC–CV charging trajectory. The feedback-based system introduces visible current spikes and higher ripple content, which can increase thermal stress and accelerate battery degradation. The MPC maintains a smooth current profile with minimal transient disturbances, thereby improving charging quality and reducing stress on the battery.

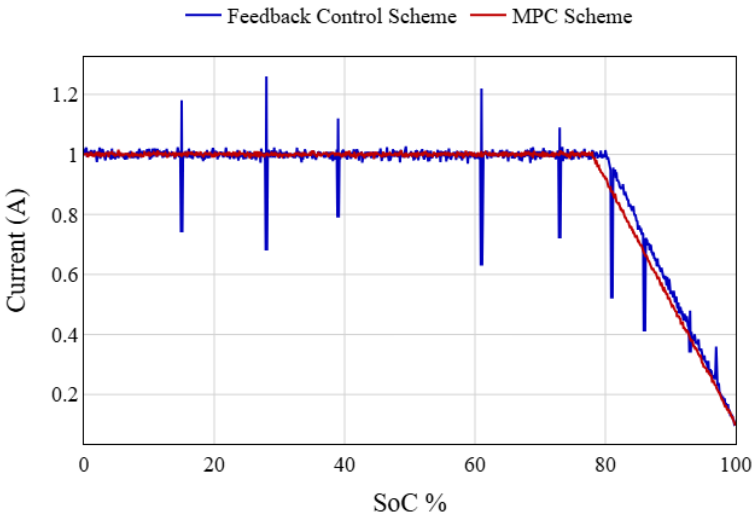



**Figure 22.** Comparison of feedback-based control and MPC schemes in simulation showing output current ($I_{out}$) over the full charging cycle, highlighting smoother current regulation under MPC and the presence of transient spikes under feedback control.

### *7.6. Loss and Performance Trade-Off Analysis*

A system-level comparison of losses and performance indicators is presented in the radar chart of Figure 23. The MPC outperforms the feedback-based controller across multiple metrics, including switching losses, conduction losses, control spikes, output current ripples, loss of ZVS and thermal performance.

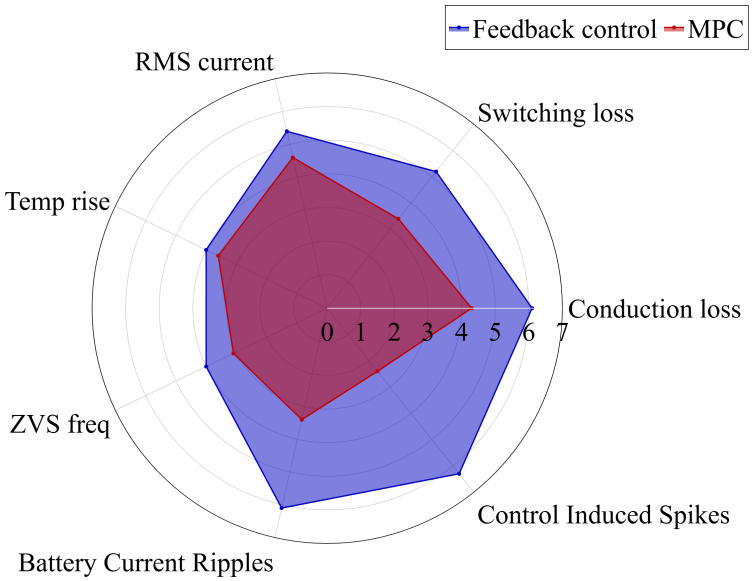



**Figure 23.** Radar chart comparison of feedback-based control and MPC schemes across seven performance metrics, highlighting overall system-level performance improvement under MPC.

The improved efficiency is primarily attributed to more consistent ZVS conditions and reduced RMS current stress. Smooth phase-shift control enables operation closer to optimal soft-switching conditions, thereby reducing switching losses, while lower current ripple minimizes conduction losses in both the converter and WPT coils. Additionally, reduced oscillatory behavior limits unnecessary circulating currents, further improving thermal performance.

## 8. Conclusions

This work presented a MPC strategy for a PSFB-based WPT charger for LEV, built on a data-driven battery model. MPC scheme was validated consistently in simulation and on a hardware test bench under aligned, lateral, and angular misalignment conditions. The proposed controller achieved faster convergence than popular feedback controller such as DRL based TD3-PI scheme, with reductions of 13.5%, 11.9%, and 6.2% in convergence time, while maintaining accurate CC charging over the tested SOC range. On the embedded C2000 platform, MPC required about 16% lower CPU utilization per PWM cycle and only 1 µs execution time compared with 3 µs for DRL based TD3-PI, and exhibited a more favorable resource breakdown (65.6% flash, 32.8% RAM, 1.6% compute versus 69.6%, 28%, and 2.1% for TD3-PI). A seven-metric radar-chart evaluation (lower is better, 0–7 scale) further showed that MPC achieved an average score of approximately 3.2, whereas the feedback-based controller remained at 5.5, indicating significantly lower losses, current ripple, and thermal stress. These results demonstrate that the proposed MPC offers a fast, efficient, and hardware-feasible control solution for static WPT charging under realistic SOC and misalignment variations, and provide a solid basis for future extensions to higher-power or dynamic charging scenarios.

**Author Contributions:** Conceptualization, A.A. and A.; methodology, A.A. and A.; software, A. and P.P.; validation, A.A., A. and P.P.; formal analysis, A.A.; investigation, A. and P.P.; resources, P.P., B.B. and I.T.C.; data curation, P.P.; writing—original draft preparation, A.A., A. and P.P.; writing—review and editing, B.B.; visualization, A.A. and P.P.; supervision, B.B. and I.T.C.; project administration, I.T.C.; funding acquisition, I.T.C. All authors have read and agreed to the published version of the manuscript.

**Funding:** The research received funding from MITACS Accelerate Program in collaboration with Wireless PnC Inc. Victoria, B.C., Canada.

**Data Availability Statement:** The original contributions presented in this study are included in the article. Further inquiries can be directed to the corresponding authors.

**Acknowledgments:** The authors would like to acknowledge Wireless PnC. Inc. for providing the equipment for testing purposes and the department of Electrical and Computer Engineering, University of Victoria, Canada and University of Windsor, Canada for providing the research facilities.

**Conflicts of Interest:** The research was partially funded by Wireless PnC Inc. Victoria, B.C., Canada. All authors declare that the research was conducted in the absence of any commercial or financial relationships that could be construed as potential conflicts of interest. The funder was not involved in the study design, collection, analysis, interpretation of data, the writing of this article or the decision to submit it for publication.

## References

1. Mogire, E. Light Electric Vehicles and Sustainable Transport in Urban Areas: A Bibliometric Review. *World Electr. Veh. J.* **2026**, *17*, 23–43. [CrossRef]
2. Xue, Z.; Liu, W.; Liu, C.; Chau, K.T. Critical Review of Wireless Charging Technologies for Electric Vehicles. *World Electr. Veh. J.* **2025**, *16*, 65. [CrossRef]
3. Hutchinson, L.; Waterson, B.; Anvari, B.; Naberezhnykh, D. Potential of wireless power transfer for dynamic charging of electric vehicles. *IET Intell. Transp. Syst.* **2019**, *13*, 3–12. [CrossRef]
4. Houache, M.S.E.; Yim, C.H.; Karkar, Z.; Abu-Lebdeh, Y. On the Current and Future Outlook of Battery Chemistries for Electric Vehicles—Mini Review. *Batteries* **2022**, *8*, 70. [CrossRef]
5. Grebtsov, D.K.; Kubasov, M.K.; Bernatskii, E.R.; Beliauski, P.A.; Kokorenko, A.A.; Isokjanov, S.S.; Kazikov, S.P.; Kashin, A.M.; Itkis, D.M.; Morozova, S.M. Electric Vehicle Battery Technologies: Chemistry, Architectures, Safety, and Management Systems. *World Electr. Veh. J.* **2024**, *15*, 568. [CrossRef]
6. Adaikkappan, M.; Sathiyamoorthy, N. Modeling, state of charge estimation, and charging of lithium-ion battery in electric vehicle: A review. *Int. J. Energy Res.* **2022**, *46*, 2141–2165. [CrossRef]
7. Joseph, P.K.; Elangovan, D. A review on renewable energy powered wireless power transmission techniques for light electric vehicle charging applications. *J. Energy Storage* **2018**, *16*, 145–155. [CrossRef]
8. Li, S.; Mi, C.C. Wireless Power Transfer for Electric Vehicle Applications. *IEEE J. Emerg. Sel. Top. Power Electron.* **2015**, *3*, 4–17. [CrossRef]
9. Huynh, P.S.; Ronanki, D.; Vincent, D.; Williamson, S.S. Overview and Comparative Assessment of Single-Phase Power Converter Topologies of Inductive Wireless Charging Systems. *Energies* **2020**, *13*, 2150. [CrossRef]
10. Zhou, K.; Wu, Y.; Wu, X.; Sun, Y.; Teng, D.; Liu, Y. Research and Development Review of Power Converter Topologies and Control Technology for Electric Vehicle Fast-Charging Systems. *Electronics* **2023**, *12*, 1581. [CrossRef]
11. Rayan, B.A.; Subramaniam, U.; Balamurugan, S. Wireless Power Transfer in Electric Vehicles: A Review on Compensation Topologies, Coil Structures, and Safety Aspects. *Energies* **2023**, *16*, 3084. [CrossRef]
12. Sagar, A.; Kashyap, A.; Nasab, M.A.; Padmanaban, S.; Bertoluzzo, M.; Kumar, A.; Blaabjerg, F. A Comprehensive Review of the Recent Development of Wireless Power Transfer Technologies for Electric Vehicle Charging Systems. *IEEE Access* **2023**, *11*, 83703–83751. [CrossRef]
13. Ayad Kiddm, W.; Mortazavi, S.S.; Saniei, M.; Monadi, M. Enhancing Efficiency and Regulation Current in Dynamic Wireless Charging of Electric Vehicles: Phase-Shift Control Methods in Resonant Inductive Power Transfer Systems. *IEEE Access* **2025**, *13*, 111317–111334. [CrossRef]
14. Bouanou, T.; Fadil, H.E.; Lassioui, A.; Assaddiki, O.; Njili, S. Analysis of Coil Parameters and Comparison of Circular, Rectangular, and Hexagonal Coils Used in WPT System for Electric Vehicle Charging. *World Electr. Veh. J.* **2021**, *12*, 45. [CrossRef]

15. Chen, K.; Zhao, Z. Analysis of the Double-Layer Printed Spiral Coil for Wireless Power Transfer. *IEEE J. Emerg. Sel. Top. Power Electron.* **2013**, *1*, 114–121. [CrossRef]
16. Barth, D.; Klaus, B.; Leibfried, T. Litz wire design for wireless power transfer in electric vehicles. In Proceedings of the 2017 IEEE Wireless Power Transfer Conference (WPTC), Taipei, Taiwan, 10–12 May 2017; pp. 1–4. [CrossRef]
17. Talluri, G.; Bindi, M.; Luchetta, A.; Grasso, F.; Luchetti, L.; Paolucci, L. Analysis of Power Losses due to Magnetic Shielding for Electric Vehicle Wireless Charging. In Proceedings of the 2021 IEEE 15th International Conference on Compatibility, Power Electronics and Power Engineering (CPE-POWERENG), Florence, Italy, 14–16 July 2021; pp. 1–6. [CrossRef]
18. Vinod, M.; Kishan, D.; Kannan, R.; Iqbal, A.; Mohammed Sulthan, S. Primary side control strategies for battery charging regulation in wireless power transfer systems for EV applications. *IET Power Electron.* **2024**, *17*, 941–952. [CrossRef]
19. Zeng, J.; Wu, J.; Li, K.; Yang, Y.; Hui, S.Y.R. Dynamic Monitoring of Battery Variables and Mutual Inductance for Primary-Side Control of a Wireless Charging System. *IEEE Trans. Ind. Electron.* **2024**, *71*, 7966–7974. [CrossRef]
20. Akanksha; Ahmad, A.; Chelvan, I.T. Fuzzy Logic Control for Wireless Power Transfer in Light Electric Vehicle Charging Applications. In Proceedings of the 2025 IEEE Canadian Conference on Electrical and Computer Engineering (CCECE), Vancouver, BC, Canada, 26–29 May 2025; pp. 643–648. [CrossRef]
21. Akanksha; Ahmad, A.; Chelvan, I.T.; Truong, K.D. Hybrid TD3-PI Control for Wireless Charging of Light Electric Vehicles. *IEEE J. Emerg. Sel. Top. Power Electron.* **2026**, *Early Access*. [CrossRef]
22. González-González, J.M.; Triviño-Cabrera, A.; Aguado, J.A. Model Predictive Control to Maximize the Efficiency in EV Wireless Chargers. *IEEE Trans. Ind. Electron.* **2022**, *69*, 1244–1253. [CrossRef]
23. Alkasir, A.; Abdollahi, S.E.; Abdollahi, S.R.; Wheeler, P. Enhancement of dynamic wireless power transfer system by model predictive control. *IET Power Electron.* **2022**, *15*, 67–79. [CrossRef]
24. Pillai, P.; Nguyen, J.; Balasingam, B. Performance analysis of empirical open-circuit voltage modeling in lithium-ion batteries—Part 3: Experimental results. *IEEE Trans. Transp. Electrif.* **2023**, *10*, 7258–7274. [CrossRef]
25. Ahmed, M.S.; Raihan, S.A.; Balasingam, B. A scaling approach for improved state of charge representation in rechargeable batteries. *Appl. Energy* **2020**, *267*, 114880. [CrossRef]
26. Balasingam, B. *Robust Battery Management System Design with MATLAB*; Artech House: Norwood, MA, USA, 2023.
27. Karami, Z.; Zhou, J.; Guidi, G.; Suul, J.A. Finite-Control-Set Model Predictive Control for Inductive Power Transfer Charging EV systems with Constant Voltage Load. In Proceedings of the 2023 11th International Conference on Power Electronics and ECCE Asia (ICPE 2023—ECCE Asia), Jeju Island, Republic of Korea, 22–25 May 2023; pp. 3422–3429. [CrossRef]
28. Alkasir, A.; Ehsan Abdollahi, S.; Reza Abdollahi, S.; Wheeler, P. A Primary Side CCS-MPC Controller for Constant Current/Voltage Charging Operation of Series-Series Compensated Wireless Power Transfer Systems. In Proceedings of the 2021 12th Power Electronics, Drive Systems, and Technologies Conference (PEDSTC), Tabriz, Iran, 2–4 February 2021; pp. 1–5. [CrossRef]


**Disclaimer/Publisher's Note:** The statements, opinions and data contained in all publications are solely those of the individual author(s) and contributor(s) and not of MDPI and/or the editor(s). MDPI and/or the editor(s) disclaim responsibility for any injury to people or property resulting from any ideas, methods, instructions or products referred to in the content.